

Quantitative Three-Dimensional Imaging of Heterogeneous Materials by Thermal Tomography

J. G. Sun

Nuclear Engineering Division,
Argonne National Laboratory,
Argonne, IL 60439
e-mail: sun@anl.gov

Infrared thermal imaging based on active thermal excitations has been widely used for nondestructive evaluation (NDE) of materials. While the experimental systems have remained essentially the same during the last few decades, development of advanced data-processing methods has significantly improved the capabilities of this technology. However, many limitations still exist. One fundamental limitation is the requirement, either explicitly or implicitly, of the tested material to be homogeneous such that detected thermal contrasts may be used to determine an average material property or attributed to flaws. In this paper, a new thermal tomography (TT) method is introduced, which for the first time can evaluate heterogeneous materials by directly imaging their thermal-property variations with space. It utilizes one-sided flash thermal-imaging data to construct the three-dimensional (3D) distribution of thermal effusivity in the entire volume of a test sample. Theoretical analyses for single and multilayer material systems were conducted to validate its formulation and to demonstrate its performance. Experimental results for a ceramic composite plate and a thermal barrier coating (TBC) sample are also presented. It was shown that thermal diffusion is the primary factor that degrades the spatial resolution with depth for TT; the spatial resolutions in the lateral and axial directions were quantitatively evaluated. [DOI: 10.1115/1.4033998]

Keywords: thermal tomography, three-dimensional imaging, pulsed thermal imaging, thermal effusivity

Introduction

Infrared thermal imaging (or thermography) based on active thermal excitations has been widely used for NDE of engineering materials and for medical imaging. Two of the most used technologies are pulsed (or flash) and modulated (or lock-in) thermal imaging, and many variations of these exist. Active thermal imaging applies an external thermal excitation on a sample surface and analyzes the surface temperature response acquired by an infrared camera. Although infrared sensing technology has been improved greatly and built into state-of-the-art infrared cameras, thermal-imaging experimental systems have remained essentially the same over the last few decades. The advancement in thermal-imaging technologies has been represented by the development of advanced data-processing methods that can more accurately measure material properties or detect defects.

A thermal-imaging system may be configured in a “reflection” mode where both the heat source and infrared camera are placed on the same side of a sample (it should be noted that in this configuration, the infrared camera does not actually detect the internal thermal reflection but only the thermal emission from the front surface), or in the transmission mode where the heat source and infrared camera are on the opposite side. Data-processing methods for these modes are different. Because the thermal excitation is typically applied on the entire surface of a test sample, which generates a nearly one-dimensional (1D) heat propagation into the

depth of the material, data-processing methods are almost all based on 1D theories or algorithms. The transmission mode has been mostly used by pulsed thermal imaging for the purpose of determining a property, usually the thermal diffusivity, with a known thickness of the material. The data-processing methods are normally based on the theory of Parker et al. [1] for single-layer materials and its extension for multilayer materials [2,3]. The fundamental assumption in these theories is that the material is homogeneous throughout the thickness or in each layer of a multilayer material. Transmission thermal imaging can also be used to detect defects and estimate defect characteristics (such as delamination gap width) if the base material is considered to be homogeneous [4].

One-sided reflection-based systems are used in most thermal-imaging applications. Their advantages include simple system setup and capability to determine material variations or defects at different depths. Data-processing methods have been developed for measuring material properties and for detecting defects. In modulated thermal imaging, the amplitude decay (with depth) and the phase shift of measured thermal waves are related to a material property (thermal diffusivity) and the excitation frequency. These relationships can be used to predict thickness-averaged material properties [5] or defect characteristics [6]. In pulsed thermal imaging, which is the most widely used technique because of its fast test speed, several data-processing methods are available. For material property measurement, regression methods based on theoretical solutions for homogeneous materials are usually used to model experimental data, and thermal properties of single- or multilayer materials can be determined [4,7]. For defect detection and characterization, data-processing methods [8–10] are designed to extract and/or enhance a thermal contrast, which can be “positive” or “negative” depending on the characteristics of the base and defect materials. The thermal contrast may be attributed to a defect only when the base material is considered homogeneous.

Contributed by the Heat Transfer Division of ASME for publication in the JOURNAL OF HEAT TRANSFER. Manuscript received March 5, 2012; final manuscript received June 17, 2016; published online July 19, 2016. Assoc. Editor: Ali Khounsary.

The United States Government retains, and by accepting the article for publication, the publisher acknowledges that the United States Government retains, a nonexclusive, paid-up, irrevocable, worldwide license to publish or reproduce the published form of this work, or allow others to do so, for United States government purposes.

The need for contrast enhancement is critical especially when detecting deeper defects because the contrast decreases rapidly with defect depth (inverse third power) [11].

The quantitative data that can be derived from current thermal-imaging methods are usually the thickness-averaged thermal diffusivity (α) and the defect depth (L) (or sample thickness). They are determined from a fundamental relationship, $t_c \propto L^2/\alpha$ or its equivalent, that exists in pulsed thermal imaging [12], where t_c is a characteristic thermal-transient time. While t_c can be measured directly from experiment, one of the two parameters (α and L) has to be known in order to determine the other. These methods are therefore applicable only to homogeneous materials, and only one parameter can be determined from each experiment.

For quantitative analysis of heterogeneous materials, the distribution of a material property within the 3D volume is required, which is usually achieved by a tomography method. Tomography, by definition [13], is a method to produce 3D image of the internal structures of a 3D object through the use of a penetrating wave (or energy). It therefore may simultaneously determine both material property and its 3D spatial distribution. A standard tomography method is the X-ray computed tomography (CT), which utilizes the X-ray transmission data through the object from multiple directions (projections) to reconstruct a transmission parameter (related to material property) distribution within the spatial domain (2D or 3D) [14]. Transmission tomography methods based on similar reconstruction principles have been developed in many fields, including optical [15], ultrasonic [16], and thermal [17,18]. These methods are generally not as mature and robust as X-ray CT. For the thermal methods [17,18], for example, only theoretical simulations were demonstrated because of the difficulty to perform the experiments. Besides transmission tomography, one-sided, reflection-based tomography methods have also been developed. Because reflection data contain information for both the magnitude of a material parameter (or discontinuity) as well as the distance of the reflection site within the object (through time of flight relationship), collected reflection data may be used directly to construct a 3D image of the object without the need of multiple-projection measurements as in the transmission tomography. Reflection-based tomography methods include confocal microscopy [19], optical coherence tomography [19], and ultrasonic scanning [14]. However, a tomography method that can produce a 3D material property distribution based on one-sided, pulsed thermal imaging has not been developed.

This paper introduces a new data-processing method for quantitative 3D thermal imaging: the TT method. It uses one-sided pulsed thermal-imaging data to construct the spatial distribution of thermal effusivity within a sample volume. In the following sections, data acquisition and analysis for pulsed thermal imaging is briefly reviewed first. Basic TT formulation is then derived. The TT performance for resolving material properties and spatial dimensions is validated based on theoretical analyses for

multilayer materials. Experimental results are presented to demonstrate data analysis procedure and data interpretation for real samples. Advantages and issues related to the current algorithm are then discussed.

Pulsed Thermal Imaging

Pulsed thermal imaging is based on monitoring the temperature decay on a sample surface after it is applied with a pulsed thermal energy that is gradually transferred inside the sample. The test setup for one-sided pulsed thermal imaging is illustrated in Fig. 1. The infrared camera used in this study is Phoenix (FLIR Systems, Inc., Wilsonville, OR), which contains a cooled focal plane array of 320×256 pixels that are sensitive in the wavelength range of $3\text{--}5\text{ }\mu\text{m}$ with a noise equivalent temperature difference of $<25\text{ mK}$. The flash system is Balcar Source ASYM 6400 (Balcar, France) that has a maximum output power of 6400 J per flash with a characteristic flash duration of $\sim 2\text{ ms}$. Pulse thermal imaging may be used to examine all the solid materials that have reasonable emissivity (say >0.5) or can be applied with a high-emissivity coating on their exposed surface, and the maximum imaging spatial resolution on the surface may potentially reach the infrared wavelength in the $5\text{ }\mu\text{m}$ range with currently available commercial optics (although spatial resolution may degrade rapidly with depth due to thermal diffusion as explained later). When pulsed thermal energy is applied (by a flash lamp), a thin layer of material on the surface is heated instantaneously to a high temperature. Heat transfer then takes place from the heated surface to the interior of the sample, resulting in a continuous decrease of the surface temperature. The infrared camera, with proper calibration, captures the surface temperature evolution during the entire thermal-transient period. The acquired thermal-imaging data therefore consist of a series of 2D images of the sample's surface temperature at consecutive time instants. This data set can be expressed as $T(x, y, t)$, where T is the surface temperature, (x, y) is the surface spatial coordinate, and t is the time. It is obvious that $T(x, y, t)$ is a 3D data set in which the time t domain is related to the depth z domain within the test sample.

In pulsed thermal imaging, the thermal excitation applied by flash lamps is typically uniform over a large surface area, which results in a predominantly 1D heat transfer in the depth direction. Therefore, most data-processing methods perform 1D analysis in the time domain, based on theoretical heat-transfer models, to retrieve depth-related information such as variation of material properties or presence of defects below each surface position. Because thermal-imaging data already have 2D spatial resolution in (x, y) , an 1D analysis for all surface positions completes the evaluation of the entire sample volume $(x, y, z(t))$.

The theoretical models used in thermal-imaging analyses are usually based on the solutions of the 1D heat conduction equation

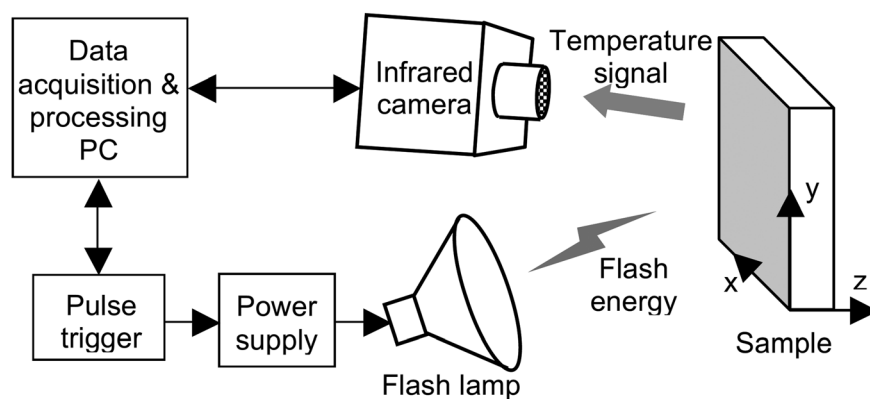


Fig. 1 Schematic of pulsed thermal-imaging test setup

$$\rho c \frac{\partial T}{\partial t} = \frac{\partial}{\partial z} \left(k \frac{\partial T}{\partial z} \right) \quad (1)$$

where $T(z, t)$ is the temperature, ρ is the density, c is the specific heat, k is the thermal conductivity, t is the time, and z is a coordinate in the depth direction ($z=0$ is the surface that receives flash heating). The initial temperature is constant (assumed to be $T=0$), and the boundaries for all the surfaces are insulated. All the material properties are assumed constant (in each material layer).

Two solutions of Eq. (1) are particularly useful for thermal imaging (and for the development of the TT method): one for a semi-infinite material and the other for a plate with a constant thickness. Under ideal pulsed thermal-imaging conditions, i.e., the pulsed heating is instantaneous and absorbed within a surface layer of negligible thickness, the solution of Eq. (1) for a semi-infinite material ($0 \leq z < \infty$) is [20]

$$T(z, t) = \frac{Q}{(\rho c k \pi t)^{1/2}} \exp\left(-\frac{z^2}{4\alpha t}\right) \quad (2)$$

where Q is the pulsed energy absorbed on the surface $z=0$ at $t=0$, and $\alpha (= k/\rho c)$ is the thermal diffusivity. The solution of Eq. (1) for a finite-thickness plate ($0 \leq z \leq L$) is [1]

$$T(z=0, t) = \frac{Q}{\rho c L} \left[1 + 2 \sum_{n=1}^{\infty} \exp\left(-\frac{n^2 \pi^2}{L^2} \alpha t\right) \right] \quad (3)$$

In Eq. (2), the (combined) material property $(\rho c k)^{1/2}$ is the thermal effusivity e . Equation (2) can thus be rewritten as

$$e = \frac{Q}{T(z=0, t) \sqrt{\pi t}} \quad (2a)$$

For heterogeneous materials, thermal effusivity e is a function of depth z , i.e., $e(z)$. For this general case, an “apparent thermal effusivity” [20], $e_a(t)$, is defined as

$$e_a(t) = \frac{Q}{T(t) \sqrt{\pi t}} \quad (4)$$

where $T(t) = T(z=0, t)$ is the surface temperature at surface position (x, y) that is measured by an infrared detector (a pixel in an infrared imager array) during a pulsed thermal-imaging test. Equation (4), therefore, converts the measured surface temperature into the apparent thermal effusivity $e_a(t)$ which, in general, differs from the material’s thermal effusivity e . For semi-infinite homogeneous materials with constant effusivity e , $e_a(t)$ is a constant and equals to e , while for heterogeneous materials with variable material effusivity along depth $e(z)$, $e_a(t)$ is a function of time (and x, y) and differs from the spatial function $e(z)$.

TT Method

The purpose of the TT method is to reconstruct the measured surface temperature in the time domain into the material’s thermal effusivity in the spatial domain. As stated above, this is equivalent as to determining $e(z)$ from $e_a(t)$. To achieve this, we need to establish the relationship between the heat-propagation time t and depth z and to construct a formulation between $e_a(t(z))$ and $e(z)$.

TT Formulation. It is well known that heat transfer is a diffusion process that does not exhibit a characteristic speed like that in a wave-propagation process. However, because thermal energy is indeed propagated during heat transfer, there should exist a relationship between the propagation distance of an equivalent thermal “front” and time. In modulated thermal imaging, for example,

the time taken for the thermal-wave crest to travel a depth z from surface ($z=0$) was found to be $t_{\text{peak}} = z^2/2\alpha$, which was determined by differentiating a thermal-wave solution with respect to time and equating to zero [21]. In pulsed thermal imaging, a correlation also exists between a characteristic time (t_c) in surface temperature evolution and the depth of a discontinuity (L): $t_c \propto L^2/\alpha$. This correlation has been the foundation used in all the empirical models to determine defect depth. Although several correlations were derived (with different correlation constants) [12], a generic relationship was found to be $t_c = L^2/(\pi\alpha)$, which was derived from Eq. (3) under the constraint $d^2(\ln T)/d(\ln t)^2 = 0$ [12]. This derivation reflects the fact that the surface temperature derivative in the log scale, $d(\ln T)/d(\ln t)$, is a constant when heat is propagating within a uniform material (see Eq. (2a)) and it changes only when an internal interface or a back surface is approached so the time t_c is directly related to the interface depth. This characteristic time t_c may be considered as the time taken for the pulsed thermal front to reach depth L . The thermal front may be defined based on the peak temperature gradient $-\partial T/\partial z$ within the material. From Eq. (2), it can be shown that the peak is located at $z_p = (2\alpha t)^{1/2}$ obtained by setting $\partial^2 T/\partial z^2 = 0$ (it propagates at same speed as the modulated waves mentioned above). By combining t_c and z_p , we may define the pulsed thermal front location at $(\pi/2)^{1/2} z_p$, which is slightly ahead of the peak temperature gradient location z_p . In the TT method, the characteristic relationship is generalized to be valid for all the depths when thermal diffusivity α is a constant [22]

$$z = (\pi \alpha t)^{1/2} \quad (5)$$

When thermal diffusivity α is not a constant but a function of depth z , Eq. (5) may be replaced by

$$t = \int_0^z \frac{2z}{\pi \alpha} dz \quad (5a)$$

Equation (5) (and (5a)) is considered the general relationship between depth z and time t for the thermal-front-propagation in a solid during pulsed thermal imaging. It indicates that the thermal-front-propagation “speed” $dz/dt = (\alpha \pi/4t)^{1/2}$ is not a constant but decreases with time. This result therefore explains the difficulty in using thermal imaging to probe deep materials, because of the gradual reduction of the thermal-front-propagation speed with depth, in addition to a drastic contrast reduction [11]. The material parameter that determines the thermal-front-propagation speed is the thermal diffusivity α .

The final step in the development of the TT method is to construct a formulation between the measured apparent effusivity $e_a(t)$ and the (unknown) material effusivity $e(z)$. Because $e_a(t)$ is determined from measured surface temperature, which results from the interaction between the heat propagation and the material property $e(z)$, the relationship between $e_a(t)$ and $e(z)$ should be in a convolution form. This situation is similar to that in electronic signal measurement, where the measured signal $s(t)$ is related to the true signal $u(t)$ by a convolution formulation: $s(t) = \int v(t-\tau)u(\tau)d\tau$, with $v(t)$ as the response function of the measurement instrument [23]. While an exact formulation for thermal imaging is difficult, if possible, to be derived directly from first principles, an approximate formulation has been found [22]

$$e_a(t) = \int_0^z z^{-1} e(\zeta) d\zeta \quad (6)$$

It is apparent that the term z^{-1} represents the response function in conventional convolution formulation. Equation (6) has a closed-form solution for $e(z)$

$$e(z) = \frac{d[ze_a(t)]}{dz} \quad (7)$$

However, when diffusivity α varies with depth, Eq. (7) is not directly usable because z is an implicit function of t as shown in Eq. (5a). Under this condition, Eq. (7) is replaced by

$$e(t) = \frac{d[\sqrt{t}e_a(t)]}{d\sqrt{t}} \quad (7a)$$

and this time function $e(t)$ is converted to the depth function $e(z)$ by using Eq. (5a). An example for evaluating Eq. (5a) for layered materials is presented later.

Equations (4)–(7) are the basic formulation for the TT method. Equations (5) and (7) are used when material's thermal diffusivity α is a constant, whereas Eqs. (5a) and (7a) are used when diffusivity is a known function of depth. These equations allow for efficient reconstruction of the thermal effusivity $e(z)$ distribution (profile) along the material depth z from the measured surface temperature $T(t)$ at each surface position. When this process is repeated for all the surface positions (x, y) , the TT method converts the measured surface temperature $T(x, y, t)$ into a 3D distribution of thermal effusivity within the sample volume $e(x, y, z)$. For completeness, this general formulation is

$$e(x, y, z) = \frac{d}{dz} \left[\frac{zQ}{T(x, y, t)\sqrt{\pi t}} \right] \quad (7b)$$

where z and t are related by Eq. (5). The absorbed heat Q may be determined in two ways. First, a calibration sample with known thermal properties may be placed at the same sample location to directly measure Q following the procedure as described in Ref. [1]. Second, because material property may be known at some depths, say at the surface, then the surface effusivity $e(z=0)$ is known and can be used to calculate Q (the same procedure may be used if the material property is known at a particular depth). The second approach is more convenient to use in practice. In all the applications, the surface optical emissivity needs to be determined prior to the surface temperature measurement.

Because the TT formulation was not derived from first principles, it needs to be validated for typical material systems evaluated by thermal imaging. One of the most difficult heterogeneity conditions for thermal imaging is layered materials, which have abrupt property changes at interfaces. In the following, we will first examine the general properties of the TT formulation for one- and two-layer materials. These properties include the conservation of total effusivity and the asymptotic behavior of the effusivity solution. Detailed evaluation of the TT performance will be presented in the next section (Performance of TT Method).

For a one-layer material, the theoretical solution for the semi-infinite condition is shown in Eq. (2) and for the finite-thickness condition in Eq. (3). For a two-layer material, the surface temperature solution for the semi-infinite case is [21]

$$T(t) = \frac{Q}{e_1\sqrt{\pi t}} \left[1 + 2 \sum_{n=1}^{\infty} \Gamma^n \exp\left(-\frac{n^2 L_1^2}{\alpha_1 t}\right) \right] \quad (8)$$

where $\Gamma = (e_1 - e_2)/(e_1 + e_2)$, and subscript 1 is for the layer near surface and 2 for that in deeper depth. The surface temperature solution for a finite-thickness two-layer material is [20]

$$T(t) = \frac{Q}{\rho_1 c_1 L_1 + \rho_2 c_2 L_2} [1 + S(t)] \quad (9)$$

where $S(t)$ is a summation expression of exponential functions of time t similar to those in Eq. (3) but with complex eigenfunction coefficients; details of this summation are not needed in this study.

Total Effusivity Conservation. We first examine the total effusivity conservation for finite-thickness one- and two-layer

materials. The total effusivity E of a material system is defined as: $E = \int_0^{\infty} e(\zeta) d\zeta$. From Eqs. (4)–(6), we have

$$E = \int_0^{\infty} e(\zeta) d\zeta = \lim_{z \rightarrow \infty} [ze_a(t)] = \lim_{t \rightarrow \infty} \frac{\sqrt{\alpha} Q}{T(t)} \quad (10)$$

For a one-layer material with constant material properties, the surface temperature is expressed in Eq. (3). It is apparent that $T(t) \rightarrow Q/(\rho c L)$ as $t \rightarrow \infty$. Therefore, $E = eL$, the correct total effusivity for the one-layer material system.

For a two-layer material system with the surface temperature expression in Eq. (9), the total effusivity E in general cannot be determined directly from Eq. (10) because the thermal diffusivity in the two layers may be different. Here, we only examine a simplified case of equal diffusivity for both layers, i.e., $\alpha = \alpha_1 = \alpha_2$. Under this condition, Eq. (9) leads to $T(t) \rightarrow Q/(\rho_1 c_1 L_1 + \rho_2 c_2 L_2)$ as $t \rightarrow \infty$; therefore, $E = e_1 L_1 + e_2 L_2$ from Eq. (10), the correct total effusivity for the two-layer material system.

Asymptotic Thermal Effusivities. The effusivity solution $e(z)$ at two asymptotic positions $z = 0$ and ∞ (or $t = 0$ and ∞) is examined for one- and two-layer material systems. The correct asymptotic values for $e(z)$ are listed in Table 1. To facilitate the derivation, the following effusivity expression is used:

$$e(z) = \frac{d}{d\sqrt{t}} \left[\frac{Q}{\sqrt{\pi T(t)}} \right] \quad (11)$$

For a semi-infinite one-layer material with surface temperature solution in Eq. (2), it is trivial to show that $e(z) = e$, a constant at all depths.

For a finite-thickness one-layer material with solution in Eq. (3), because $T(t)$ approaches a constant as $t \rightarrow \infty$, Eq. (11) then leads to $e(\infty) = 0$. At $z = 0$, we note

$$\begin{aligned} \lim_{t \rightarrow 0} \sum_{n=0}^{\infty} \exp\left(-\frac{\pi^2 \alpha t}{L^2} n^2\right) &= \lim_{t \rightarrow 0} \sum_{n=0}^{\infty} \Delta n \exp\left(-\frac{\pi^2 \alpha t}{L^2} n^2\right) \\ &= \frac{L}{2\sqrt{\pi \alpha t}} \text{erf}(\infty) \end{aligned} \quad (12)$$

where $\Delta n = 1$ and erf is the error function with $\text{erf}(\infty) = 1$. It therefore follows from Eqs. (3), (11), and (12) that $e(0) = e$.

For a semi-infinite two-layer material with solution in Eq. (8), it is apparent that $T(t) \rightarrow Q/(e_1\sqrt{\pi t})$ as $t \rightarrow 0$; Eq. (11) therefore leads to $e(0) = e_1$. As $t \rightarrow \infty$, it is noted that all the exponential terms within the summation become unity. Using the equation $\sum_{n=0}^{\infty} \Gamma^n = (1 - \Gamma)^{-1}$, it then can be shown that $T(t) \rightarrow Q/(e_2\sqrt{\pi t})$ as $t \rightarrow \infty$; therefore $e(\infty) = e_2$.

For a finite-thickness two-layer material with solution in Eq. (9), because $T(t)$ approaches a constant as $t \rightarrow \infty$, Eq. (11) leads to $e(\infty) = 0$. At $z = 0$, however, it is difficult to evaluate the summation term $S(t)$ to verify $e(0) = e_1$. Instead, numerical solutions presented in the next section (Performance of TT Method) will demonstrate this result.

In the above analyses, we have shown that the TT formulation does satisfy the total effusivity conservation as well as determine correct effusivity values at the asymptotic positions $z = 0$ and ∞ for one- and two-layer material systems. The analyses can be

Table 1 List of correct asymptotic $e(z)$ values for various material systems

Material system	$e(0)$	$e(\infty)$
Semi-infinite one-layer	e	e
Finite one-layer	e	0
Semi-infinite two-layer	e_1	e_2
Finite two-layer	e_1	0

easily extended to material systems with more than two layers. These results therefore serve as a validation of the TT formulation for general applications. The performance of the TT formulation to predict detailed effusivity depth distribution is presented in the next section (Performance of TT Method).

Performance of TT Method

The performance of the TT method was evaluated by reconstruction of thermal effusivity depth profiles of multilayer materials that are common in engineering structures. These material systems have abrupt changes in material properties. The challenge is to resolve both the abrupt changes at interfaces and the constant thermal properties within all the layers. Most heterogeneous materials exhibit only gradual property variation along depth, so the performance and accuracy of the TT method would be better for typical heterogeneous materials than for multilayer materials. In the following, examples for one-, two-, and three-layer materials are presented. Table 2 lists the three sets of material properties, identified as materials nos. 1, 2, and 3, that we used.

For a single-layer material, the surface temperature $T(t)$ in Eq. (3) can be used to calculate the thermal effusivity profile $e(z)$ from Eqs. (4)–(7). For this calculation, we assumed that the material is no. 1 with a thickness of 10 mm. Because the front surface, which is an interface ($e(0^+) = e$ and $e(0^-) = 0$), is naturally resolved and the material property is constant, the TT

performance is evaluated on the basis of the depth resolution at the back surface. Figure 2(a) plots the material effusivity profile $e(z)$ predicted by the TT method. The real material effusivity distribution used in the simulation is also plotted in the figure. To facilitate the visualization of the result, the material system is considered as a plate, so that a cross-sectional image (e.g., in the x – z plane) of the material's thermal effusivity can be displayed, as shown in Fig. 2(b). It is seen that the predicted effusivity is equal to the real effusivity in shallow depths, but deviates from the real at depths near the back surface interface at $z = 10$ mm. The exact depth of the back surface is located at 46% of the material effusivity in the predicted profile. The reduced resolution (or blurring) at the back surface is due to the thermal diffusion to be discussed later. Nevertheless, the predicted effusivity profile does follow the sharp boundary and reduces to zero at depths $z > 16$ mm (approaching the asymptotic solution $e(\infty) = 0$). In addition, the area under the predicted effusivity profile is equal to the area of the real effusivity profile, because of the conservation of total effusivity.

For a two-layer system, we assumed that the first layer contains material no. 1 with a thickness of 1 mm, and the second layer contains material no. 2 with a thickness of 10 mm. The theoretical solution of the surface temperature response under pulsed thermal-imaging condition can be obtained from an analytical solution (Eq. (9)) or a numerical method [7]. Figure 3 shows the predicted material effusivity profile and cross section image as compared

Table 2 List of thermal properties for three postulated materials used in examples

Material no.	Conductivity, k (W/m K)	Heat capacity, ρc (J/m ³ K)	Diffusivity, α (mm ² /s)	Effusivity, e (J/m ² K s ^{1/2})
1	2	2×10^6	1	2000
2	1	1×10^6	1	1000
3	$2^{1/2}$	$2^{-1/2} \times 10^6$	2	1000

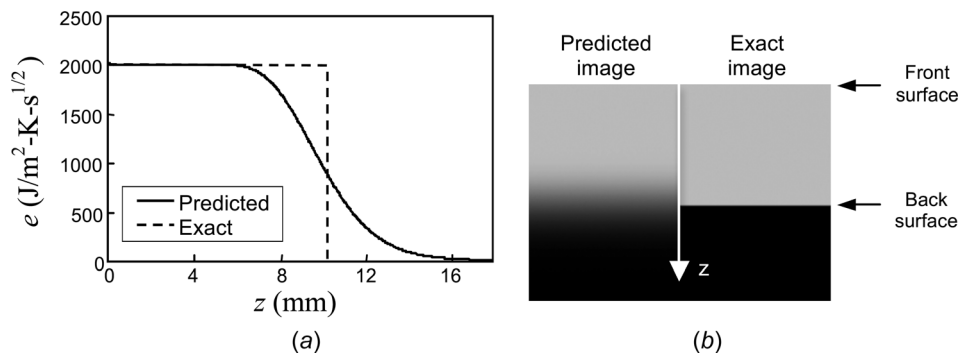


Fig. 2 Predicted and exact material effusivity (a) profiles and (b) cross section images as a function of depth for a single-layer system

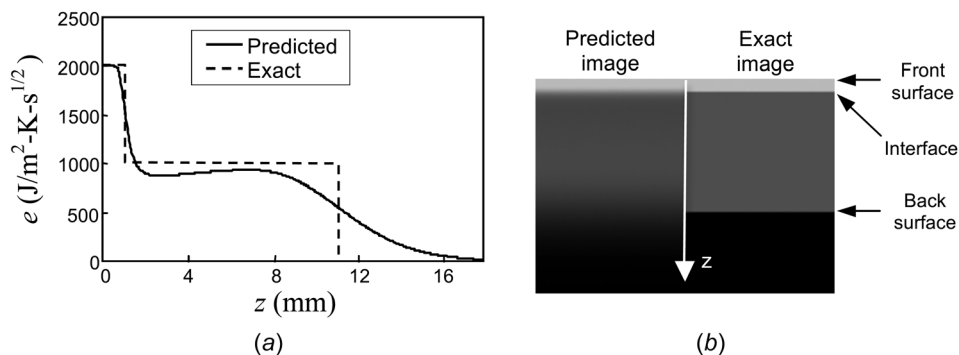


Fig. 3 Predicted and exact material effusivity (a) profiles and (b) cross section images as a function of depth for a two-layer system

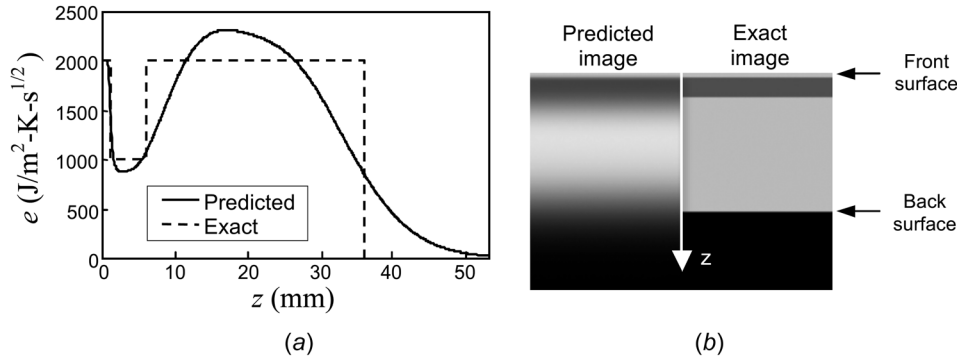


Fig. 4 Predicted and exact material effusivity (a) profiles and (b) cross section images as a function of depth for a three-layer system

with those of the real material effusivity for the two-layer system. It is evident that the predicted effusivity values in both layers are well reproduced. Again, the predicted profile exhibits diffusion around sharp boundaries, which is more apparent at greater depths. The diffusion also causes an overshoot of the predicted effusivity change between the layers and a delayed recovery of effusivity in the second layer, although the exact effusivity of the second layer is obtained if the thickness of the second layer is >20 mm [22].

For the three-layer system, we assumed that the first and third layers consist of material No. 1, the second layer consists of material No. 2, and the thickness for the layers is 1, 5, and 30 mm, respectively. The predicted material effusivity profile and cross section image are shown in Fig. 4. Again, the predicted effusivity profile reproduces well the exact distribution, although with reduced resolution and some deviation of effusivity changes around interfaces due to thermal diffusion. The exact effusivity of the third layer is recovered if its thickness is >60 mm [22]. This example can be considered as a simulation for the detection of an embedded material (the second layer) within a uniform material (layers 1 and 3).

The theoretical results presented in Figs. 2–4 demonstrate that the TT method is robust and stable for analyzing single and multi-layer materials. Both material property and depth of the layers can be determined simultaneously. These results also confirm the conservation of total effusivity and accurate prediction of layer effusivity values under asymptotic conditions.

The above examples are for layered materials with a constant thermal diffusivity. To illustrate the effect of diffusivity variation, we repeat the two- and three-layer simulations by replacing the material no. 2 with no. 3, which has a higher thermal diffusivity as listed in Table 2. While the thermal effusivity time profile $e(t)$ is readily constructed from Eq. (7a), the relationship between t and z can be derived from Eq. (5a) for a general multilayer material with the layer number $N \geq 2$

$$t = \frac{z^2}{\pi\alpha_1}, \quad \text{for } 0 < t < t_1 \quad (13a)$$

$$t = \sum_{i=1}^{n-1} \frac{z_i^2}{\pi} \left(\frac{1}{\alpha_i} - \frac{1}{\alpha_{i+1}} \right) + \frac{z_n^2}{\pi\alpha_n}, \quad \text{for } t_{n-1} < t < t_n, \quad n = 2, \dots, N \text{ and } t > t_N \quad (13b)$$

where

$$t_1 = \frac{z_1^2}{\pi\alpha_1} \quad (14a)$$

$$t_n = \sum_{i=1}^{n-1} \frac{z_i^2}{\pi} \left(\frac{1}{\alpha_i} - \frac{1}{\alpha_{i+1}} \right) + \frac{z_n^2}{\pi\alpha_n}, \quad n = 2, \dots, N \quad (14b)$$

Figure 5 shows a comparison of the predicted thermal effusivity depth profiles $e(z)$ for two- and three-layer materials with matched or unmatched thermal diffusivities. It is evident that all the predicted profiles are good approximations of the respective exact profiles shown in Figs. 3(a) and 4(a). The shape and magnitude of the predicted profiles are dominated by the material's thermal effusivity while the depth dimension is controlled by thermal diffusivity. Therefore, it is necessary to know the thermal diffusivities of all the material layers when constructing 3D spatial thermal effusivity images from experimental data. If the diffusivities are unknown so thermal effusivity images based on $e(t)$ from Eq. (7a) are constructed, we may still estimate the material's thermal effusivities but with a lesser certainty to layer thicknesses because $t^{1/2}$ may no longer be proportional to depth z for layers 2 and beyond.

Experimental Results

TT can be used in all the material-characterization applications that currently employ pulsed thermal imaging. In this section, experimental results are presented for two material systems: a ceramic matrix composite (CMC) plate and a TBC sample.

In practical applications, the constructed 3D effusivity $e(x,y,z)$ is normally presented as 100 2D effusivity images (slices) at $z = \text{constant}$ planes: $e(x,y,z_1), e(x,y,z_2), \dots, e(x,y,z_{100})$. The depth as well as the thickness (Δz) of each slice can be determined from Eq. (5). However, because the thermal diffusivity α is usually unknown and may vary with depth, each slice is therefore constructed based on a fixed time scale, i.e., $\Delta z \sim (t_{\text{exp}})^{1/2}/100$, where t_{exp} is the test duration. As a result, the thickness of all the slices is the same for a homogeneous material. The thickness of the slices for heterogeneous materials is generally different but can be

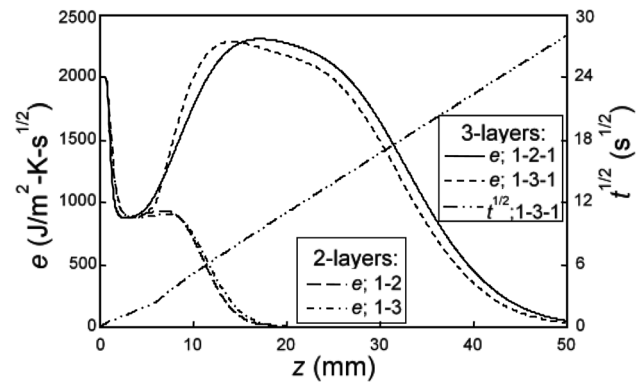


Fig. 5 Predicted thermal effusivity $e(z)$ profiles for two- and three-layer material systems (e.g., 1 and 2 indicate that the first- and second-layer materials are Nos. 1 and 2, respectively) and a time $t^{1/2}$ profile for a three-layer system

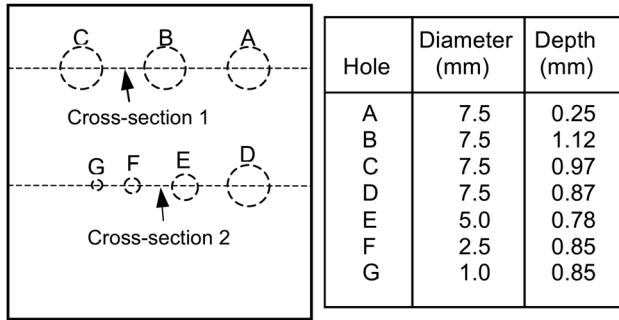


Fig. 6 Diagram and hole dimensions of a flat-bottom-hole plate (dimensions of 5 cm \times 5 cm with thickness between 2.3 and 2.7 mm)

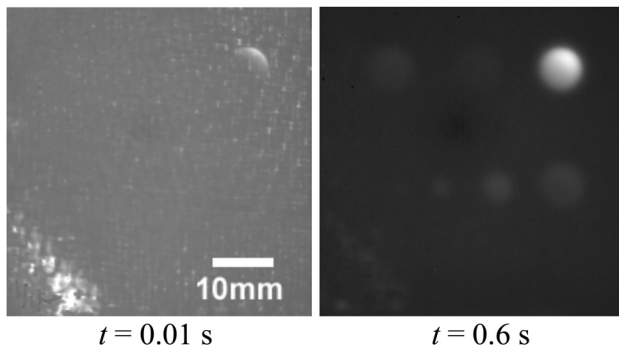


Fig. 7 Thermal images taken at $t = 0.01$ and 0.6 s after thermal flash from front surface of a CMC plate with machined flat-bottom holes at back surface

determined from Eq. (5) if the local thermal diffusivity is known. In multilayer materials, for example, the thermal diffusivity in each layer is a constant, so the thickness of all the slices in each layer is the same.

CMC. CMCs are advanced materials being developed for high-temperature structural applications, such as the thermal protection system in spacecrafts and components in turbine engines [4,24]. The critical flaw in CMCs is delamination. Pulsed thermal imaging is a preferred NDE method to detect delaminations in CMCs. The detection sensitivity as a function of delamination size and depth is normally determined by using calibration plate samples with machined flat-bottom holes at the back surface to simulate the delaminations. The CMC plate used in this study has seven machined flat-bottom holes of various diameters and depths from the back surface, as illustrated in Fig. 6. The depth of the holes in

Fig. 6 is the distance from the hole bottoms to the front flat surface where thermal-imaging data were acquired. The plate dimensions are 5 cm \times 5 cm, and its thickness varies from 2.3 to 2.7 mm. The composite plate was not completely densified, so it contained many small cracks and distributed porosities within its interior.

Pulsed thermal-imaging data (surface temperature images) were obtained from the front flat surface of the plate by using the system illustrated in Fig. 1. The imaging rate was 516 Hz, with a total of 3000 frames taken for a test duration of 5.8 s. Each image has 256×200 pixels which correspond to a surface area resolution of 0.25×0.25 mm² per pixel, and the maximum temperature rise during the flash period was ~ 40 K. Figure 7 shows two typical thermal images taken at 0.01 and 0.6 s after the flash. Although all the holes can be detected from the latter thermal image, the thermal contrast of the deeper holes is weak and could easily become unidentifiable. It is also noted that there are many large shallow defects located at the lower-left corner of this sample.

The 3D distribution of the thermal effusivity for this CMC plate was constructed using Eqs. (4)–(7). Based on the experimental parameters and material properties, each plane slice for this plate has a thickness of 0.042 mm. The 3D effusivity distribution was then sliced in plane and vertical cross sections to display the internal structures of the sample. Figure 8 shows plane slices at four depths below the front surface. All the flat-bottom holes are visible; they show darker grayscale because the material within the holes at those planes is air, which has a very low-effusivity value. These holes usually become visible at slightly shallower depths than their actual depths due to the thermal diffusion effect mentioned earlier; the exact depths can be located when the effusivity value drops to 46% of the base material effusivity (see Fig. 2(a)). These plane slices also reveal many defects (with lower effusivity). The small distributed defects are mostly voids due to incomplete densification of the plate. The large defects located at the lower-left corner are observed in the shallow slices at $z = 0.26$ and 0.59 mm; they produced artifacts (overshoots) in deeper slices ($z = 0.87$ and 1.2 mm) due to thermal diffusion effect.

Figure 9 shows the predicted cross-sectional effusivity images and the corresponding cross-sectional diagrams along the two horizontal lines indicated in Fig. 6. These cross-sectional images are the first of their kind being produced by a thermal-imaging method, and they make data interpretation and analysis much easier. It is evident that the depths of all the flat-bottom holes as well as the back surface of the plate are well resolved (note that all the holes have an inclined bottom surface due to a machining error). In addition, the depth distribution of many small defects is resolved, especially in the shallow depths. These cross section images also reveal the thermal diffusion effects in both depth (axial) and lateral directions: the lateral diffusion caused an apparent expansion of the hole diameter along depth; the depth diffusion is represented by the increased blurring of the back surface of deeper holes and the plate. The TT data in Fig. 9 can be used to quantitatively evaluate these effects.

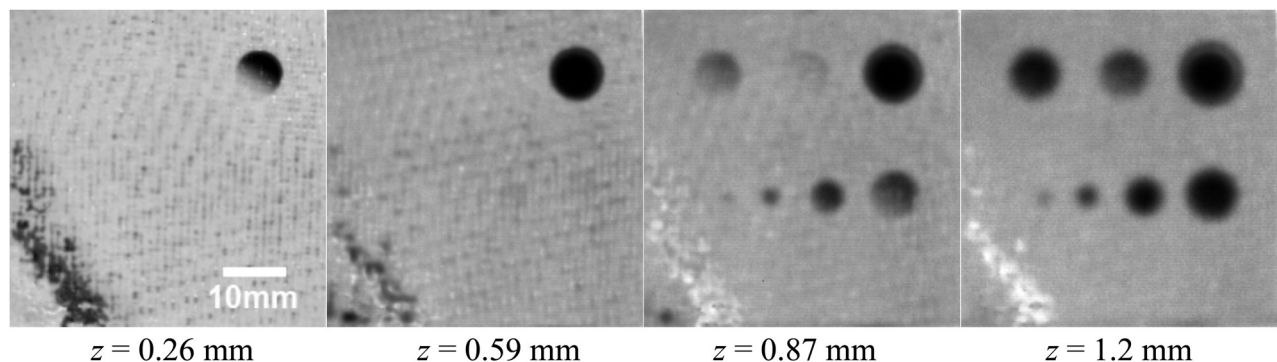


Fig. 8 Plane thermal effusivity images at various depths below the front surface of a CMC plate with machined flat-bottom holes at back surface

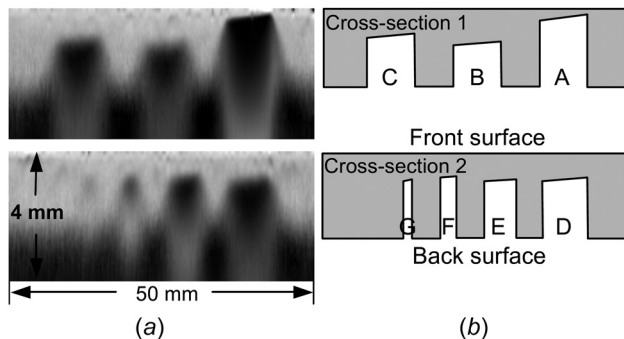


Fig. 9 (a) Cross-sectional thermal effusivity images and (b) corresponding diagrams along the horizontal lines of the flat-bottom-hole plate as illustrated in Fig. 5

Multilayer TBC. TBCs are commonly used on hot gas-path components in air- and land-based gas turbines. In this application, a thermally insulating ceramic topcoat (the TBC) is bonded to a thin oxidation-resistant metal coating (the bond coat) on a metal substrate. As a result, TBC-coated components can be operated at higher temperatures, with improved performance and extended lifetime [25]. Because TBCs play a critical role in protecting the substrate components, it is important to detect damage and property change in early stages of coating degradation to ensure coating integrity.

A 25-mm-diameter TBC sample was imaged by TT. The imaging rate was 1068 Hz with a total of 3000 frames taken. Each image has 128×128 pixels which correspond to a surface area resolution of $0.2 \times 0.2 \text{ mm}^2$ per pixel. This sample was exposed to a high temperature for many thermal cycles, so small cracks had developed within the ceramic coating. The thickness is 0.35 mm for the ceramic topcoat and 3.2 mm for the substrate. The nominal thermal effusivity e is 2010 and $5490 \text{ J/(m}^2 \text{ K s}^{1/2})$, and the

thermal diffusivity α is 0.498 and $2.49 \text{ mm}^2/\text{s}$ for the coating and substrate, respectively. The bond coat is thin and has properties similar to the substrate, so it is considered as part of the substrate. Figure 10(a) shows a typical cross-sectional effusivity image of the sample. It clearly displays a low-effusivity coating layer with some effusivity variations and a relatively uniform high-effusivity substrate layer. Based on the material properties and test duration, the thickness of each plane slice is $21 \mu\text{m}$ within the coating layer and an average of $47 \mu\text{m}$ within the substrate, as determined from Eq. (5). In Fig. 10(b), the average effusivity profile from the measured results is compared with that calculated from a theoretical two-layer model using the TBC material properties. Clearly, the measured profile matches well with the theoretical one. The slight difference in shallow depths (early times) is due to variations in experimental and coating conditions, such as flash duration and surface roughness, and in greater depths to a low signal-to-noise ratio (this noise is visible in Fig. 10(a)). These deviations could be reduced with more accurate system calibration and robust signal smoothing.

Figure 11 shows plane effusivity images at different depths within the sample. They clearly indicate the presence of small damages (with lower effusivity) with sizes of 1 mm and smaller at depths below the half thickness of the coating layer ($0.2\text{--}0.35 \text{ mm}$). The effusivity variation near the edge, as seen in the 1.2-mm-depth image, was due partially to a slight difference of coating thickness and thermal property at the edge (because the edge was mounted during the thermal cycling test) and partially to the use of a single flash lamp (located at left side) in the thermal-imaging test. These results demonstrate that TT can determine material property as well as detect and locate small damages within TBC coatings.

Discussion

TT is the first practical thermal-imaging method for quantitative 3D imaging of the interior of a solid sample. It has significant

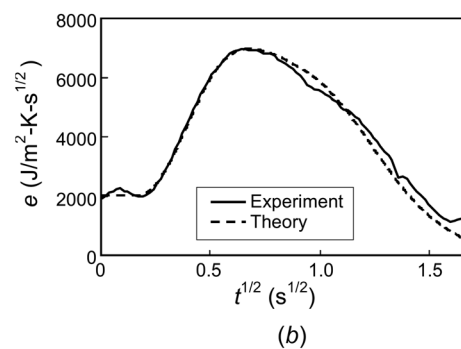
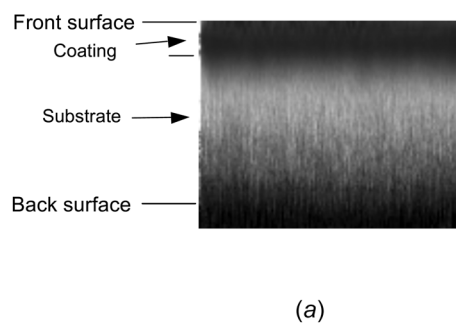


Fig. 10 (a) Cross section effusivity image and (b) effusivity depth profile for TBC sample

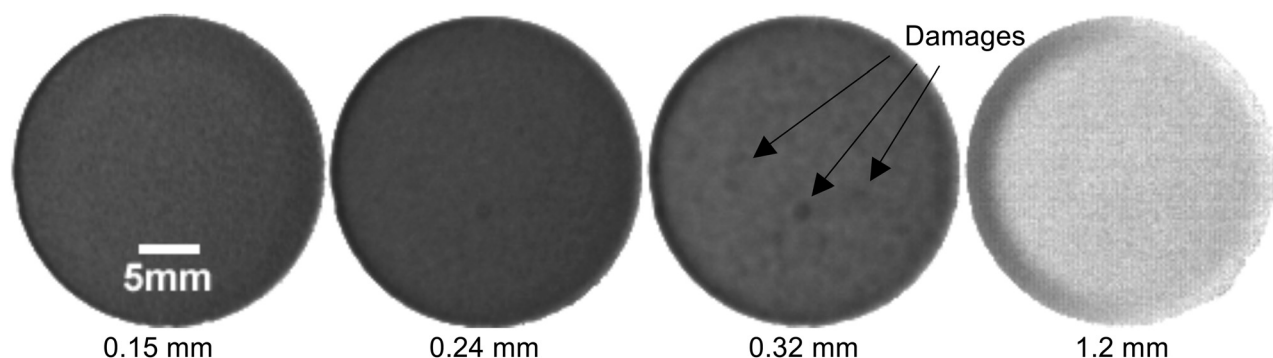


Fig. 11 Plane effusivity images at various depths of TBC sample

advantages over conventional contrast-based methods [26]. This is because that the constructed parameter from TT is a physical property that is inherent to each material, so multiple materials within a heterogeneous material can be easily identified. When data analysis is performed by 2D plane slicing or 3D volume rendering, material compositions/structures and flaws as well as their dimensions within the 3D volume can be determined simultaneously. As a result, data analysis and interpretation become much easier.

Thermal diffusion is inherent to all heat-transfer processes and is considered as the single factor that limits the detection sensitivity of all the thermal-imaging methods. This limitation is characterized by the “rule of thumb” for active thermal imaging: the diameter of the smallest detectable discontinuity should be larger than its depth under the surface [11,27]. Formally, this rule stipulates that for a discontinuity of diameter D at a depth z below surface, the discontinuity can only be detected by thermal imaging when $D > z$. The current TT method was not designed specifically to deal with thermal diffusion, which would require the development of a diffusion-related response function instead of z^{-1} in Eq. (6); diffusion therefore affects the TT prediction accuracy. In Fig. 9, the cross-sectional images for a CMC plate with flat-bottom holes, the lateral diffusion caused apparent increase of hole diameter in greater depths, while the axial (depth) diffusion caused increased blurring of the back surface with depth. Axial diffusion may also produce other artifacts, such as the overshoot beneath an interface (Figs. 2(a) and 4). In practical applications, however, lateral diffusion is of a lesser concern because thermal imaging is usually used for relatively thin materials. The axial diffusion is more important to TT; its effect is discussed and evaluated below.

The axial diffusion effect can be determined quantitatively based on the TT reconstruction for a single-layer material, as shown in Fig. 2. In this material system, the back surface (at $z = 10$ mm) is the only location where thermal diffusion is observed. The diffusion causes a resolution degradation that can be evaluated using the effusivity derivative $-de/dz$. Ideally, if the effusivity profile was exact, the back surface would be a discontinuity so $-de/dz = \delta$ (Dirac delta function) at $z = 10$ mm. In reality, as shown in Fig. 12, the $-de/dz$ curve has a broad distribution around the back surface, indicating a poor resolution there. The spatial resolution is normally characterized by the full width at half maximum, which was found to be $0.46z$ where z is the depth of the discontinuity. Therefore, the depth resolution for the current TT method is $0.46z$; it degrades linearly with depth. Physically, the resolution represents the depth range within which two separate discontinuities cannot be differentiated by the method. Combined with the known lateral resolution stipulated by the rule of thumb for all the thermal-imaging methods, the lateral and axial resolutions at depth z for the TT method are therefore $>z$ and $0.46z$, respectively.

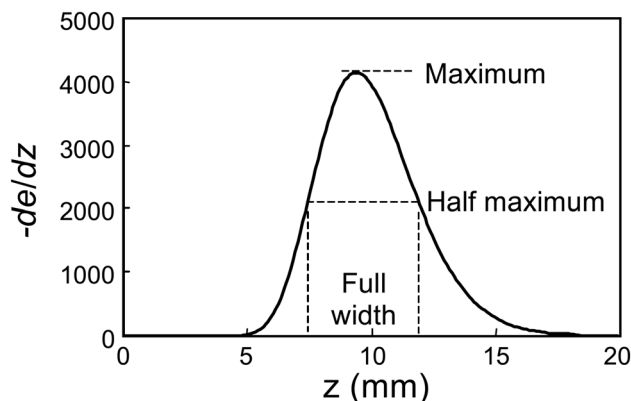


Fig. 12 Effusivity derivative curve as a function of depth for a one-layer material with a material effusivity of $2000 \text{ J/(m}^2 \text{ K s}^{1/2})$ and a thickness of 10 mm

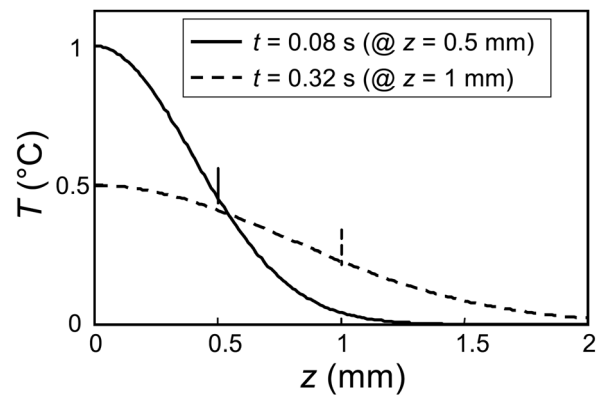


Fig. 13 Temperature distributions within a semi-infinite material at various times after a thermal flash is applied on $z = 0$ at $t = 0$

Thermal diffusion is a unique phenomenon not observed (or insignificant) in other imaging technologies. In ultrasonic testing, for example, the spatial resolution is determined by the shape and width of the ultrasonic pulses. These pulse characteristics generally do not change in the far field [28], so the spatial resolution is maintained for a long distance of pulse propagation. In thermal imaging, the thermal front degrades quickly as the heat is propagated inside a material. This degradation can be observed from the temperature distributions within a semi-infinite material at various times, as expressed in Eq. (2). Figure 13 shows two such distributions calculated based on the properties of material no. 1 in Table 2. For each distribution, the nominal propagation distance z determined from Eq. (5) is also marked in the figure. At $t = 0$, the temperature distribution, not shown in Fig. 13, is a Dirac delta function $\delta(0)$, so it has an infinitely sharp thermal front at $z = 0$. As time increases, the thermal front becomes broader with a decreased “intensity” (slope), which imposes a weaker driving force to the front so its propagation speed decreases as predicted by Eq. (5).

Because of thermal diffusion, thermal energy has been considered a poor source to probe materials. Nevertheless, thermal imaging is a very effective technique especially for large-area imaging of relatively thin materials. Recent advances in infrared camera manufacturing have also significantly improved its accuracy and accessibility. The challenge to expand this technology therefore relies on our ability to eliminate the diffusion effect so imaging sensitivity and resolution are maintained at all the conditions. A recent study has demonstrated that the axial thermal diffusion can be accounted for and eliminated under certain conditions [29]. It is therefore possible that further development may eventually break the rule of thumb that limits all the current thermal-imaging methods and will establish TT as a high-resolution imaging tool for not only NDE but also other scientific, medical, and engineering imaging applications.

Conclusion

A TT method was developed to construct for the first time the 3D thermal effusivity distribution in the entire volume of a test sample based on one-sided pulsed thermal-imaging data. Because thermal effusivity is an intrinsic material property that is unique for each material, TT may quantitatively characterize material compositions and dimensions of various components within the 3D sample volume. The TT formulation was found to satisfy the total effusivity conservation as well as to yield correct asymptotic values for single-layer and multilayer material systems. Theoretical calculations verified that TT can predict the material effusivity as a function of depth, although the accuracy is limited around the interfaces of abrupt property changes due to thermal diffusion. Experimental TT results were presented for two samples: a CMC

plate with machined flat-bottom holes and a multilayer TBC. Data analyses were carried out from 2D slice images in the plane (parallel to surface) and cross section directions. It was demonstrated that TT can determine material properties and resolve the distributed defects within the volume of the samples. These theoretical and experimental evaluations showed that TT results can be easily interpreted and analyzed. Although thermal diffusion is a problem for high-resolution imaging by the current TT method which has the lateral and axial resolutions of $>z$ and $0.46z$, respectively, at depth z , advanced algorithms to eliminate this effect are being developed. These advances will further establish TT as a high-resolution imaging tool for not only NDE but also other scientific, medical, and engineering applications.

Acknowledgment

This work was sponsored by the U.S. Department of Energy, Office of Fossil Energy, Advanced Research and Technology Development/Materials Program, and by the Heavy Vehicle Propulsion Materials Program, DOE Office of FreedomCAR and Vehicle Technology Program, under Contract No. DE-AC05-00OR22725 with UT-Battelle, LLC.

Nomenclature

- c = specific heat (J/kg K)
 e = thermal effusivity ($\text{J/m}^2 \text{K s}^{1/2}$)
 e_a = apparent thermal effusivity ($\text{J/m}^2 \text{K s}^{1/2}$)
 k = thermal conductivity (W/m K)
 L = plate thickness (m)
 N = number of layers
 Q = pulsed energy absorbed on surface (J/m²)
 S = a function with summation terms
 t = time (s)
 T = temperature ($^{\circ}\text{C}$ or K)
 x, y, z = x -, y -, z -coordinates (m)

Greek Symbols

- α = thermal diffusivity (m^2/s)
 Γ = dimensionless parameter: $(e_1 - e_2)/(e_1 + e_2)$
 ρ = density (kg/m^3)

Subscripts

- 1, 2 = for layers 1 and 2
 c = characteristic

References

- [1] Parker, W. J., Jenkins, R. J., Butler, C. P., and Abbott, G. L., 1961, "Flash Method of Determining Thermal Diffusivity, Heat Capacity, and Thermal Conductivity," *J. Appl. Phys.*, **32**(9), pp. 1679–1684.
- [2] Bulmer, R. F., and Taylor, R., 1974, "Measurement by the Laser Flash Method of Thermal Diffusivity in Two-Layer Composite Samples," *High Temp. High Pressures*, **6**(5), pp. 491–497.
- [3] Hartmann, J., Nilsson, O., and Fricke, J., 1993, "Thermal Diffusivity Measurements on Two-Layered and Three-Layered Systems With the Laser-Flash Method," *High Temp. High Pressures*, **25**(4), pp. 403–410.
- [4] Sun, J. G., 2007, "Evaluation of Ceramic Matrix Composites by Thermal Diffusivity Imaging," *Int. J. Appl. Ceram. Technol.*, **4**(1), pp. 75–87.
- [5] Bennett, T. D., and Yu, Y., 2005, "A Nondestructive Technique for Determining Thermal Properties of Thermal Barrier Coatings," *J. Appl. Phys.*, **97**(1), p. 013520.
- [6] Busse, G., 2001, "Lockin Thermography," *Nondestructive Handbook, Infrared and Thermal Testing*, 3rd ed., X. Maldague and P. O. Moore, eds., ASNT Press, Columbus, OH, Chap. 11, Part 4.
- [7] Sun, J. G., 2010, "Method for Analyzing Multi-Layer Materials From One-Sided Thermal Imaging," U.S. Patent No. 7,769,201.
- [8] Maldague, X., and Marinetti, S., 1996, "Pulsed Phase Infrared Thermography," *J. Appl. Phys.*, **79**(5), pp. 2694–2698.
- [9] Rajic, N., 2002, "Principal Component Thermography for Flaw Contrast Enhancement and Flaw Depth Characterisation in Composite Structures," *Compos. Struct.*, **58**(4), pp. 521–528.
- [10] Shepard, S. M., Lhota, J. R., Rubadeux, B. A., Wang, D., and Ahmed, T., 2003, "Reconstruction and Enhancement of Active Thermographic Image Sequences," *Opt. Eng.*, **42**(5), pp. 1337–1342.
- [11] Maldague, X., 2001, "General Approaches and Techniques of Infrared and Thermal Testing," *Nondestructive Handbook, Infrared and Thermal Testing*, 3rd ed., Vol. 40, X. Maldague and P. O. Moore, eds., ASNT Press, Columbus, OH, Chap. 2, Part 2.
- [12] Sun, J. G., 2006, "Analysis of Pulsed Thermography Methods for Depth Prediction," *ASME J. Heat Transfer*, **128**(4), pp. 329–338.
- [13] Merriam-Webster, 2015, Merriam-Webster Online Dictionary, <http://www.merriam-webster.com/dictionary/tomography>, Merriam-Webster, Inc., Springfield, MA.
- [14] Kak, A. C., and Slaney, M., 1988, *Principles of Computerized Tomographic Imaging*, IEEE Press, New York.
- [15] Inaba, H., 1993, "Coherent Detection Imaging for Medical Laser Tomography," *Medical Optical Tomography: Functional Imaging and Monitoring*, G. J. Muller, ed., SPIE, Bellingham, WA, pp. 317–347.
- [16] Simonetti, F., 2009, "Modern Ultrasound Imaging: An Exciting Window Into the Sub-Surface World," *Review Quantitative Nondestructive Evaluation*, Vol. 28, D. O. Thompson and D. E. Chimenti, eds., American Institute of Physics, Melville, NY, pp.33–46.
- [17] Bakirov, V. F., Kline, R. A., and Winfree, W. P., 2003, "Multiparameter Thermal Tomography," *Review of Quantitative Nondestructive Evaluation*, Vol. 23, D. O. Thompson and D. E. Chimenti, eds., American Institute of Physics, Melville, NY, pp. 461–468.
- [18] Kolehmainen, V., Kaipio, J. P., and Orlande, H. R. B., 2007, "Reconstruction of Thermal Conductivity and Heat Capacity Using a Tomographic Approach," *Int. J. Heat Mass Transfer*, **50**(25–26), pp. 5150–5160.
- [19] Liu, Z. P., Sun, J. G., and Pei, Z. J., 2011, "Cross-Polarization Confocal Imaging of Subsurface Flaws in Silicon Nitride," *Int. J. Appl. Ceram. Technol.*, **8**(2), pp. 411–422.
- [20] Balageas, D. L., Krapez, J. C., and Cielo, P., 1986, "Pulsed Photothermal Modeling of Layered Materials," *J. Appl. Phys.*, **59**(2), pp. 348–357.
- [21] Lau, S. K., Almond, D. P., and Patel, P. M., 1991, "Transient Thermal Wave Techniques for the Evaluation of Surface Coatings," *J. Phys. D*, **24**(3), pp. 428–436.
- [22] Sun, J. G., 2008, "Method for Thermal Tomography of Thermal Effusivity From Pulsed Thermal Imaging," U.S. Patent No. 7,365,330.
- [23] Press, W. H., Teukolsky, S. A., Vetterling, W. T., and Flannery, B. P., 1992, *Numerical Recipes in C*, 2nd ed., Cambridge University Press, Cambridge, UK, p. 538.
- [24] Roth, D. J., Jacobson, N. S., Gray, J. N., Cosgriff, L. M., Bodis, J. R., Wincheski, R. A., Rauser, R. W., Burns, E. A., and McQuater, M. S., 2005, "NDE for Characterizing Oxidation Damage in Reinforced Carbon-Carbon Used on the NASA Space Shuttle Thermal Protection System," *Ceram. Eng. Sci. Proc.*, **26**(2), pp. 133–141.
- [25] Feuerstein, A., and Bolcavage, A., 2004, "Thermal Conductivity of Plasma and EBPVD Thermal Barrier Coatings," 3rd International Surface Engineering Conference, pp. 291–298.
- [26] Sun, J. G., 2013, "Analysis of Data Processing Methods for Pulsed Thermal Imaging Characterization of Delaminations," *Quant. Infrared Thermogr. J.*, **10**(1), pp. 9–25.
- [27] Roth, D. J., Bodis, J. R., and Bishop, C., 1997, "Thermographic Imaging for High-Temperature Composite Materials—A Defect Detection Study," *Res. Nondestruct. Eval.*, **9**(3), pp. 147–169.
- [28] Bray, D. E., and Stanley, R. K., 1997, *Nondestructive Evaluation*, CRC Press, Boca Raton, FL.
- [29] Sun, J. G., 2013, "Method for Implementing Depth Deconvolution Algorithm for Enhanced Thermal Tomography 3D Imaging," U.S. Patent No. 8,465,200.